



Meteoroid Bombardment of Lunar Poles

Petr Pokorný^{1,2,3} , Menelaos Sarantos² , Diego Janches² , and Erwan Mazarico⁴

¹ Department of Physics, The Catholic University of America, Washington, DC 20064, USA; petr.pokorny@nasa.gov

² Heliophysics Science Division, NASA Goddard Space Flight Center, Greenbelt, MD 20771, USA

³ Astrophysics Science Division, NASA Goddard Space Flight Center, Greenbelt, MD 20771, USA

⁴ Solar System Exploration Division, NASA Goddard Space Flight Center, Greenbelt, MD 20771, USA

Received 2019 October 15; revised 2020 March 24; accepted 2020 March 25; published 2020 May 12

Abstract

While the floors of deep lunar craters are largely shielded from solar radiation and thus provide an ideal thermal environment for water-ice accumulation, meteoroids on highly inclined orbits can easily access permanently shadowed regions and alter the surface properties via hypervelocity impacts. Here we consider the detailed topography of the lunar poles and a dynamical model of meteoroids to quantify the meteoroid mass fluxes, energy deposition, and impact ejecta mass production rates. Our analysis of regions within 5° from the two lunar poles shows that the variations of the meteoroid mass flux, energy flux, and ejecta production rate are within 50% of their median values. We find that the lunar poles are easily accessible by meteoroid impacts, including the permanently shadowed regions. We find a positive correlation between the surface slope and the meteoroid ejecta production rate, a finding that suggests that a higher impact gardening rate on steep crater walls can facilitate mass wasting.

Unified Astronomy Thesaurus concepts: Lunar craters (949); The Moon (1692); Lunar surface (974); Lunar impacts (958); Space weather (2037); Micrometeoroids (1048)

1. Introduction

The polar regions of the Moon are interesting both from a scientific perspective, because they can provide clues to physical processes that apply to the entire solar system, as well as for human exploration, because they may contain possible space exploration resources in the form of volatiles. High resolution surface temperature maps of both lunar poles by the Lunar Reconnaissance Orbiter (LRO) Diviner instrument (Paige et al. 2010), combined with information on the topography derived from Lunar Orbiter Laser Altimeter (LOLA) observations (Smith et al. 2010), provide a unique way of characterizing permanently shadowed regions that consistently retain low temperatures and thus offer stability for water-ice deposits on the Moon over geological timescales. Hayne et al. (2015), Fisher et al. (2017), Li & Milliken (2017), and Li et al. (2018) suggested that many of the south polar permanently shadowed regions (PSRs) exhibit signatures of exposed water-ice deposits, while other PSRs lack the water-ice signatures completely. Rubanenko et al. (2019), using small crater morphology and distribution on Mercury and the Moon, suggested that water-ice is present in significantly more lunar south pole craters than previously thought from observations (Colaprete et al. 2010; Hayne et al. 2015). However, the distribution of water-ice layers was not correlated with the maximum surface temperature, where some regions such as the Shackleton or Shoemaker craters showed either an anomalously low amount or no amount of water-ice. Due to shielding from the solar wind, the most significant exogenous sources of the depletion of surface ice are expected to be local interstellar H Ly α radiation (Morgan & Shemansky 1991), mass wasting on highly inclined slopes (Fisher et al. 2017), meter-sized or larger impacts (Suggs et al. 2014), and the impacts of smaller meteoroids that are constantly bombarding the lunar poles with a broad range of impact velocities (Pokorný et al. 2019). Recent work by Deutsch et al. (2020) further supports a very patchy spatial distribution of surface ice, which suggests high overturn or destruction rates.

The objective of this work is to evaluate how the access of smaller meteoroids changes from crater to crater at high lunar latitudes. This calculation provides critical data to test whether albedo differences and/or the patchiness seen in surface ice signatures might be attributed to the differences in meteoroid impacts. Whereas the effect of impactors in the centimeter to meter scale on the gardening rate has been quantified (Gault 1973; Arnold 1975; Hurley et al. 2012), the effects of sporadic meteoroids, which are smaller but far more frequent, on the topographically complex polar regions of the Moon have not been quantified. The first high resolution dynamical model of meteoroids impacting the lunar surface, presented by Pokorný et al. (2019), provided an overview of the different physical effects that meteoroid impacts produce on the lunar surface, yet a major limitation of that investigation was its assumption of a spherical Moon geometry. Here, we expand this work by combining the meteoroid direction, velocity, mass, and flux distribution from the Pokorný et al. (2019) model with the detailed topography of lunar poles to evaluate the meteoroid flux, the total energy delivered by meteoroids, and the ejecta mass created through meteoroid impacts of micron- to millimeter-sized particles.

2. Lunar Data Sets and Meteoroid Model

In this article we focus on both lunar polar caps, specifically the region limited to selenographic latitudes between 85° and 90° (approximately 150 km from the north/south pole). For this study we use the LOLA Gridded Data Records (GDR) topography map and the sporadic meteoroid background model to quantify the effects of meteoroid impacts onto the lunar poles. Ancillary data used for this work were the Diviner depth of ice, maximum temperature, and average temperature and LOLA albedo. The links and names of all data sets used here are described in Appendix A.

We transformed the original LOLA GDR data set into a 250 m \times 250 m Cartesian grid in X , Y , with the Z component obtained using bilinear interpolation applied to the LOLA

altimeter data set. The Diviner maximum temperature, average temperature, depth of ice, and LOLA albedo maps were obtained in the form of triangles (i.e., a set of values for each triangle on the surface mesh). For each grid point in our 250 m Cartesian grid we found the relevant Diviner surface triangle and its corresponding values for our calculation (see the project GitHub page⁵ for the codes used in this article). For missing values we filled the blanks with a bilinear interpolation using four points closest to the missing grid point. Surface slopes were calculated from our gridded data set by slicing the grid squares, denoted by four vertices, into two triangles and calculating the slope as the average of the two, also keeping the triangle slope difference. For grid squares with differences higher than 0.1° , we added two more triangles (sliced in the reverse direction) and used the average of all four triangle slopes as the final value. We tested the average slope calculated using our method against the LOLA data set and 99.99% of our slopes were $<0.1\%$ different from the LOLA slope data set.

The lunar meteoroid environment model used in this work was described in detail in Pokorný et al. (2019). In this model the inner solar system is populated by meteoroids originating in four distinctive populations: main-belt asteroids (MBA), Jupiter family comets (JFC), Halley-type comets (HTC) and Oort Cloud comets (OCC). We considered particle diameters between $D = 10 \mu\text{m}$ and $D = 2000 \mu\text{m}$, with an assumed bulk density equal to 3 g cm^{-3} for the main-belt meteoroids, and 2 g cm^{-3} for cometary meteoroids. The model was calibrated with the mass influx at Earth from Carrillo-Sánchez et al. (2016) yielding a yearly average of 1.4 metric tonnes per day of material delivered onto the lunar surface from asteroidal and short-and-long cometary sources. To simulate meteoroid effects on the scale of millions of years, we calculated moments of the meteoroid input function from this model by accumulating model output over one Earth orbit around the Sun from 00:00:00 UTC, 2013 July 1, to 12:00:00 UTC 2014 June 30. These calculations combined 731 temporal slices (each 12 hr apart from the next) into one average file.

Based on Pokorný et al. (2019), we expect negligible changes in the annual average for different years due to the fact that Earth's heliocentric distance variations, which are the main contributor to the variations of the meteoroid flux at the Moon, are negligible from year to year. Because in this calculation we have marginalized the meteoroid differences experienced by a crater at different local times and months of the year, the only parameter influencing the year-to-year comparisons are the amplitudes of monthly variations due to the orbital motion of the Moon around Earth, i.e., the lunar phase at the start of a year. Pokorný et al. (2019) showed that the highest meteoroid flux occurs close to the full moon, while the minimum occurs around the new moon. The most favorable configuration (all monthly maxima are counted within the year while the last monthly minimum is not counted) versus the least favorable configuration leads to a difference of approximately 3.5% in the mass flux averaged over one year (using Equation (12) in Pokorný et al. 2019).

3. Methods

In order to map the meteoroid impacts onto the topography of the lunar poles, we binned the meteoroid radiant/sky map in

ecliptic longitude (2 degree bins), latitude (2 degree bins), and the meteoroid impact velocity at the Moon (2 km s^{-1} bins). Each of these 3D bins provides the yearly averaged mass flux, direction, and velocity allowing us to calculate the incident mass flux on each surface segment on the Moon. For simplicity we assume that the Moon has no axial tilt to avoid incorporating seasonal variations, which would increase the already computationally demanding processing part. Due to the broad range of meteoroid ecliptic latitudes, this simplification has a negligible effect on the results shown here. The small fraction of the total meteoroid flux that is very close to the ecliptic, and their shallow impact angles with respect to the polar caps, diminish the overall contribution of these low-inclination impactors.

For each surface element (triangle) we first determine whether the surface element is obstructed by any topographic feature with respect to the particular radiant point using ray-tracing methods. First, we rotate all surface elements with respect to the center of the Moon such that the incident meteoroid ray is originating from $(0, 0, Z)$ direction, i.e., the ray is only traveling in the Z direction. Then we select all the triangles that are able to shadow the inspected surface element using bounding boxes (i.e., rectangles defined by the minimum and maximum x and y values of each triangle) and the Z component of all surface elements. Then we check whether the centroid of the inspected surface element is shadowed by any of the triangles from the selected set. This procedure results in shadow maps of both polar regions for all directions available from our meteoroid model. We tested our shadowing procedure against the algorithm presented in Mazarico et al. (2018) and obtained essentially identical results.

Using the shadow maps we then determine the mass flux \mathcal{M} , energy flux \mathcal{E} , and ejecta mass production rate \mathcal{P}^+ for each surface element using the following expressions:

$$\mathcal{M} = \sum_{\lambda, \beta} M_{\text{met}}(\lambda, \beta) S(\lambda, \beta) \cos(\varphi), \quad (1)$$

$$\mathcal{E} = \sum_{\lambda, \beta, v_{\text{imp}}} \frac{1}{2} M_{\text{met}}(\lambda, \beta, v_{\text{imp}}) v_{\text{imp}}^2 S(\lambda, \beta) \cos(\varphi), \quad (2)$$

$$\mathcal{P}^+ = \mathcal{C} \sum_{\lambda, \beta, v_{\text{imp}}} M_{\text{met}}(\lambda, \beta, v_{\text{imp}}) v_{\text{imp}}^{2.46} \times (\lambda, \beta) S(\lambda, \beta) \cos^3(\varphi), \quad (3)$$

where λ and β are the Sun-centered ecliptic longitude and latitude of meteoroids, $S(\lambda, \beta)$ is the shadow map coefficient, φ is the incidence angle measured from the normal of the surface patch, v_{imp} is the meteoroid impact velocity, and $\mathcal{C} = 7.358 \text{ km}^{-2} \text{ s}^2$ is a scaling constant determined from the laboratory experiments reported by Koschny & Grün (2001). The scaling constant \mathcal{C} describes the amount of ejecta the surface produces. The value of \mathcal{C} used here characterizes impacts of glass projectiles into ice-silicate surfaces. The mass of produced ejecta, \mathcal{P}^+ , is likely orders of magnitude smaller than for solid ice surfaces, as suggested by the discrepancy of the meteoroid modeling and the Lunar Dust Experiment (LDEX) discussed in Pokorný et al. (2019). The incidence angle φ is calculated for each surface patch separately, where $\cos \varphi = -\mathbf{n}_{\text{sur}} \cdot \mathbf{e}_{\text{imp}}$, where \mathbf{n}_{sur} is the normal of the surface patch, and \mathbf{e}_{imp} is the unit velocity vector of the impacting meteoroid. Then grazing impacts have $\cos \varphi$ close to zero,

⁵ https://github.com/McFly007/AstroWorks/tree/master/Pokorny_et_al_2019_ApJ

while perpendicular impacts are close to unity. Since we only investigate the centroids (central points) of each surface triangular element, $S(\lambda, \beta)$ is either one or zero. We tested the shadowing procedure for more points (100) for each triangle for a smaller area (Shackleton crater) and the result did not yield significant differences when averaging over the entire year. The ejecta mass production rate \mathcal{P}^+ in Equation (3) is a special case of a more general equation given by Koschny & Grün (2001), which was applied in Pokorný et al. (2019) to compare to the ejecta cloud measured around the Moon by LDEX (Horányi et al. 2015).

4. Comparison of North and South Polar Regions

In this Section we present our results and compare the meteoroid environment at the two lunar polar regions. Figure 1 shows the variations of \mathcal{M} , \mathcal{E} and \mathcal{P}^+ for the south (left panels) and north (right panels) polar regions. The color ranges in Figure 1 do not show the entire range of values, but are limited to $[P_{2.275\%}, P_{97.725\%}]$, where P_x is the x th percentile of the sample. Using percentile values allows us to show the variations of each quantity over the entire region, while avoiding regions with very low values (PSR) or very high values (mountains). We do not use the mean values and standard deviations here due to the nonnormal distribution of \mathcal{M} , \mathcal{E} and \mathcal{P}^+ on the lunar poles.

Our model finds very small variations of the meteoroid mass flux, \mathcal{M} , at both poles, with median values equal to $\mathcal{M}_{S50\%} = 0.3971 \text{ g cm}^2 \text{ s}^{-1} \times 10^{-16}$ and $\mathcal{M}_{N50\%} = 0.3976 \text{ g cm}^2 \text{ s}^{-1} \times 10^{-16}$, where 95% of values represented on the north and south polar maps are within $\pm 6\%$ of the median value (see Table 1 for more details). The modeled minimum value near the south pole is $\mathcal{M}_{\min} = 0.3077 \text{ g cm}^2 \text{ s}^{-1} \times 10^{-16}$ within a small $\sim 5 \text{ km}$ crater between the Scott M and Nobile craters (Cartesian $[X = 116, Y = 130] \text{ km}$), resulting in a 22% smaller mass flux than the median value; similar results are also found at the north pole. On the other hand, the maximum modeled value at both poles is $\mathcal{M}_{\max} = 0.4151 \text{ g cm}^2 \text{ s}^{-1} \times 10^{-16}$, which is only 5% higher than the median value. This means that despite lunar polar topography and the presence of PSRs, the meteoroid mass flux is rather uniform across both polar regions, unlike the solar flux, which varies by orders of magnitude.

The modeled spatial variations of the meteoroid energy flux \mathcal{E} are very similar to those of the mass flux, where the only difference is higher energy fluxes on several ridges located between 4° – 5° away from the pole. The median values of \mathcal{E} are very similar for both poles, $\mathcal{E}_{S50\%} = 99.96$ and $\mathcal{E}_{N50\%} = 100.11 \text{ kJ cm}^{-2} \text{ s}^{-1} \times 10^{-16}$, respectively. Despite the complex topography of both lunar poles, from the variations of \mathcal{M} and \mathcal{E} we can estimate that the average impact velocity $V_{\text{imp}} = 22.4 \text{ km s}^{-1}$ provides a reasonable evaluation of meteoroid energy from the meteoroid flux at both poles. This is in agreement with the results reported by Pokorný et al. (2019), which showed in their Figure 9 that the longitudinally averaged meteoroid impact velocity is between 15 and 23 km s^{-1} , and the majority of locations on both poles are not shielded from impactors coming from slightly above or below the ecliptic. Since energy scales with the square of the incident velocity, the more energetic impactors are emphasized, thus $V_{\text{imp}} = 22.4 \text{ km s}^{-1}$ is higher than that inferred from meteoroid mass fluxes.

The increased dependence on the incidence angle φ for the meteoroid ejecta production rate \mathcal{P}^+ changes the overall appearance of polar maps. While the majority of flat regions have very similar values close to the median $\mathcal{P}_{S50\%}^+ = 2990.45$ and $\mathcal{P}_{N50\%}^+ = 2973.18 \text{ g cm}^{-2} \text{ s}^{-1} \times 10^{-16}$, all areas with higher slopes produce significantly more ejecta, which is valid even for permanently shadowed walls of craters on both lunar poles (e.g., the Shackleton crater close to the south pole). This is due to the fact that the $\cos^3(\varphi)$ scaling for areas with higher slopes emphasizes the contribution of energetic meteoroids originating from directions close to the ecliptic (the so-called apex source populated by HTC and OCC meteoroids). Unlike \mathcal{M} or \mathcal{E} , Table 1 also shows that \mathcal{P}^+ is highly asymmetric for both poles, where the first 50% of data points are concentrated very close to the median, while the regions with higher \mathcal{P}^+ values exhibit a long tail.

The Shackleton crater is a good example for understanding this effect. The minimum value of $\mathcal{P}^+ = 2743.14 \text{ g cm}^{-2} \text{ s}^{-1} \times 10^{-16}$ is localized at the floor of the crater, while the sides of the crater with high slopes (up to 32° , Zuber et al. 2012) experience 31% higher values of $\mathcal{P}^+ = 3605.42 \text{ g cm}^{-2} \text{ s}^{-1} \times 10^{-16}$. When comparing it to values in Table 1, we see that Shackleton crater experiences both extremes of the meteoroid ejecta production rate. Nevertheless, the floor of the crater is still subjected to meteoroid bombardment, despite the very high angles of incidence (28° – 32° , i.e., effectively shielding the crater floor from meteoroids with ecliptic latitudes $< 32^\circ$).

Figure 2 shows how the meteoroid ejecta production rate \mathcal{P}^+ varies with slope on the global scale. Each data point in this figure represents the value modeled at each surface patch on our maps, where the color coding is based on the maximum temperature registered at the particular location of the data point. In order to assess the trend in the data, we calculated three percentile values (5%, 50%, and 95%) using a moving window in slope with a width of 1° , taking steps of 0.5° in the range 0° – 20° , and then fitted the percentile ranges with 0° – 5° polynomials. We find that polynomials of a degree higher than second-degree do not significantly improve the fit (using a reduced χ^2 statistic with unit variance $\sigma = 1$, thus we opted for the second-degree polynomial as our fitting function for the simplicity of its parameters. Both poles show a very similar trend where the meteoroid ejecta production rate \mathcal{P}^+ for all three percentile values is well described with the second-degree polynomial. However, the south pole, due to its more diverse topography and larger permanently shadowed area, shows a larger spread of \mathcal{P}^+ values, but the quadratic trend holds for both the low and high maximum temperature areas. The north pole has a very similar envelope (5%–95% percentile range) to the south pole, but its median value grows more rapidly with increasing slope, which is due to the smaller number of highly inclined permanently shadowed areas. All coefficients for the second-degree polynomial fits are summarized in Table 2. These polynomial fits can be easily used for a quick estimate of the ejecta production rates in any model that requires such an input, e.g., a model estimating impact gardening on lunar poles. The polynomial fits of the median and the 5%–95% percentile range allow quite precise estimates without using the full-fledged model presented here.

Finally, we may look at the histograms of modeled \mathcal{M} , \mathcal{E} , and \mathcal{P}^+ to demonstrate the divergence from the normal (Gaussian) distribution that is usually assumed for various

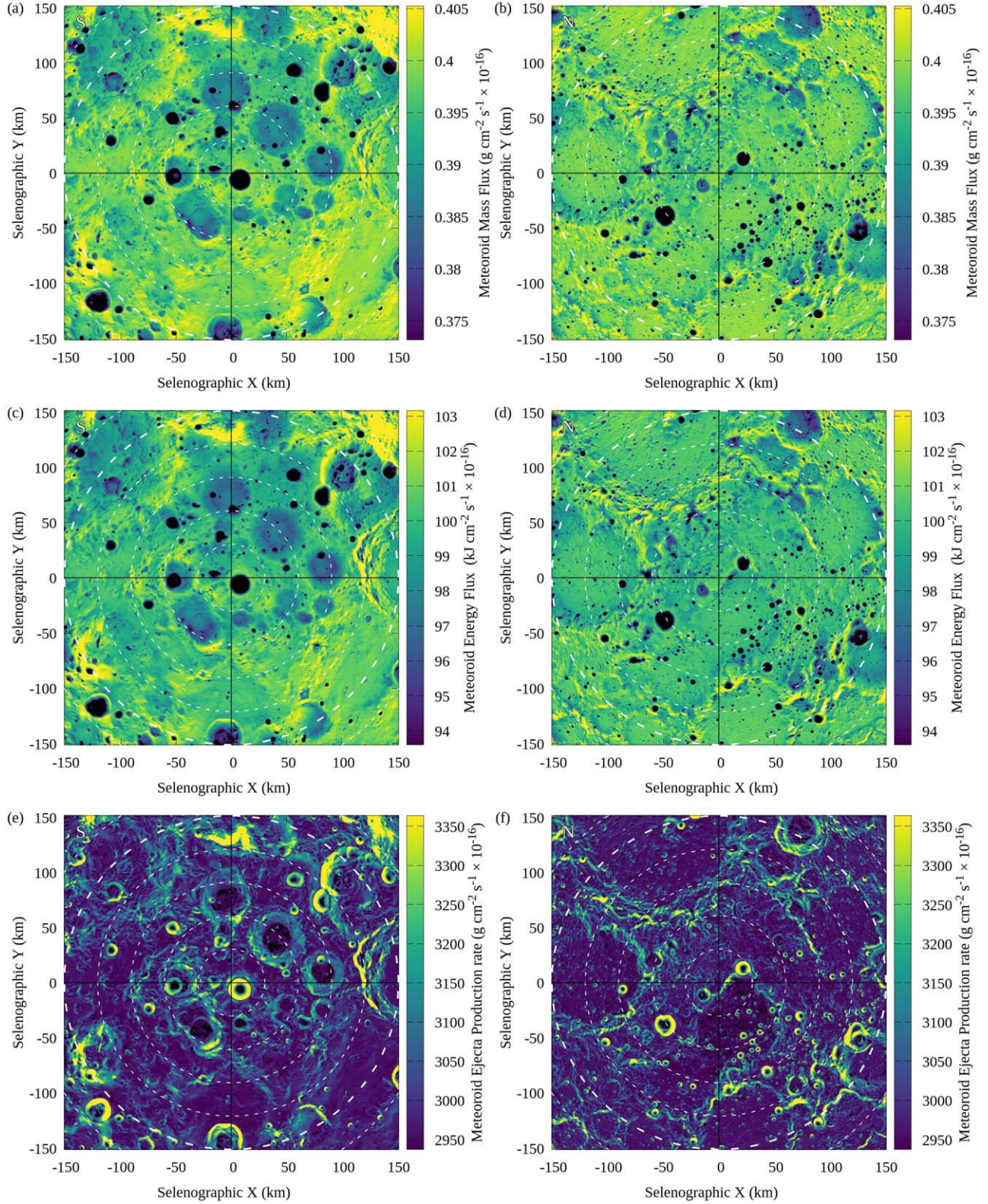


Figure 1. Left panels: south pole maps of the (a) meteoroid mass flux \mathcal{M} , (c) meteoroid energy flux \mathcal{E} , and (e) meteoroid mass ejecta production rate \mathcal{P}^+ . Right panels: north pole maps of the (b) meteoroid mass flux \mathcal{M} , (d) meteoroid energy flux \mathcal{E} , and (f) meteoroid mass ejecta production rate \mathcal{P}^+ . All maps are in gnomonic (selenographic) coordinates with a resolution of 250 m.

physical processes. Figure 3 shows that the histograms of meteoroid mass and energy fluxes are asymmetric, with a tail toward the smaller values where the function profiles show a shape similar to a Cauchy–Lorentz distribution. Frequencies of

both quantities are more dispersed for the south pole due to the more complex topography. The distribution of the meteoroid ejecta production rate \mathcal{P}^+ (right panel in Figure 3) is extremely asymmetric, where the majority of locations on both poles have

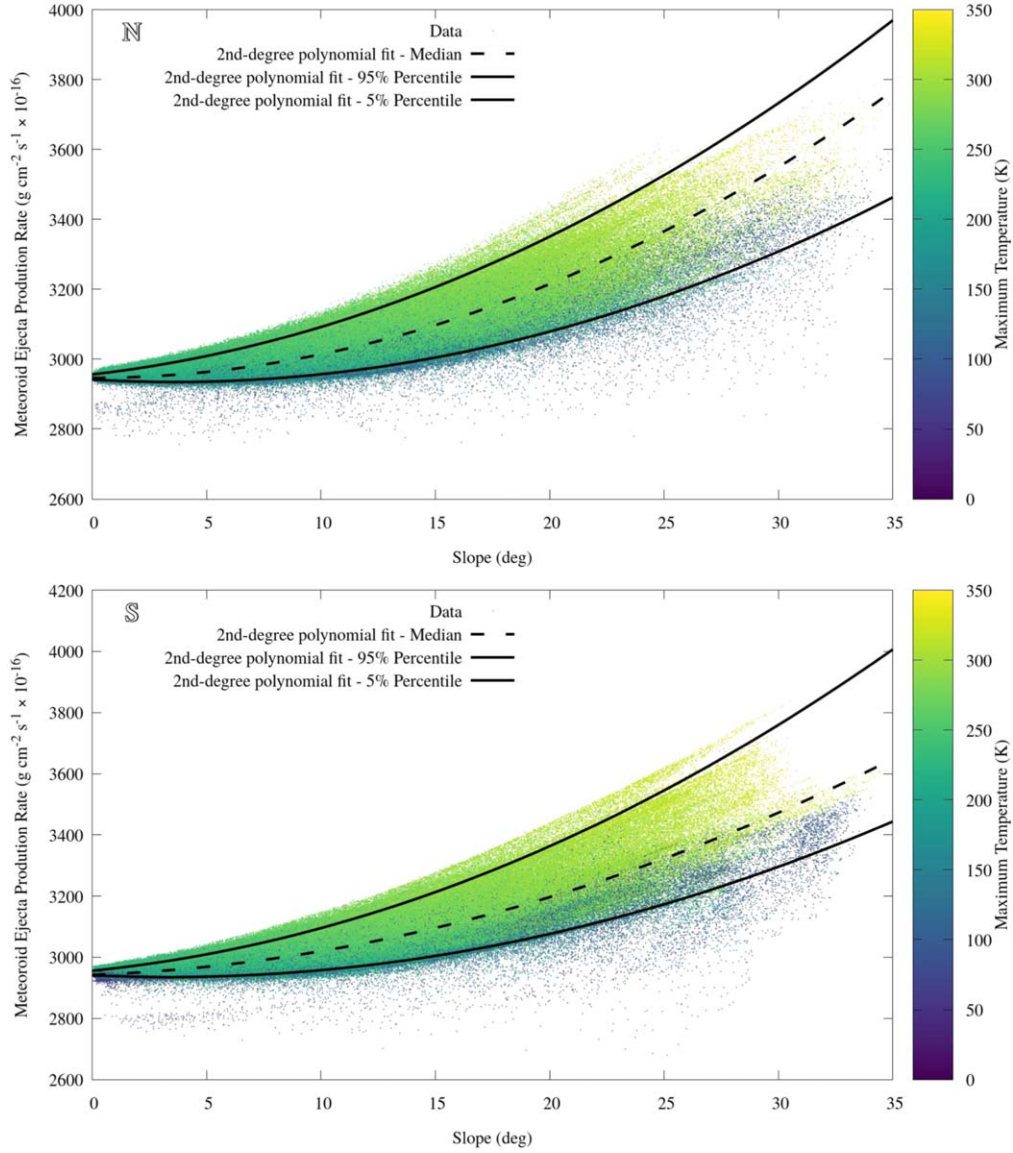


Figure 2. Top panel: meteoroid ejecta mass production rates \mathcal{P}^+ as a function of the surface slope in degrees for the lunar north pole. The color bar show the maximum surface temperature T_{\max} in kelvin. The ejecta mass production rate follows a quadratic trend with respect to the surface slope shown by the dashed black line (quadratic fit to the median value for each 0.5° bin) and solid black lines (quadratic fit to the 90% percentile range). Bottom panel: the same as the top panel but for the lunar south pole.

Table 1
Percentile Values for \mathcal{M} ($\text{g cm}^{-2} \text{s}^{-1} \times 10^{-16}$), \mathcal{E} ($\text{kJ cm}^{-2} \text{s}^{-1} \times 10^{-16}$) and \mathcal{P}^+ ($\text{g cm}^{-2} \text{s}^{-1} \times 10^{-16}$) for Both the North and South Lunar Poles

	Percentile						
	0.135%	2.275%	15.73%	50%	84.27%	97.725%	99.865%
North \mathcal{M}	0.3378	0.3740	0.3913	0.3976	0.4002	0.4031	0.4063
South \mathcal{M}	0.3310	0.3732	0.3898	0.3971	0.4009	0.4052	0.4128
North \mathcal{E}	82.027	93.832	98.444	100.11	100.95	102.32	103.95
South \mathcal{E}	79.842	93.594	97.991	99.956	101.21	103.16	106.92
North \mathcal{P}^+	2908.8	2936.7	2944.7	2973.2	3089.8	3311.2	3524.4
South \mathcal{P}^+	2904.6	2937.0	2947.9	2990.4	3119.9	3363.6	3596.5

similar values of \mathcal{P}^+ , which is also apparent from Figures 1 and 2 where the low slope ($<5^\circ$) areas are experiencing essentially the same effects of the meteoroid bombardment. To show the divergence of these distribution from normal distributions, we added the best normal distribution fits (using the least-

squares method) to \mathcal{M} , \mathcal{E} , and \mathcal{P}^+ on both poles (dashed lines in Figure 3).

The contributions of different meteoroid source populations to impact related processes on lunar poles are summarized in Table 3. The median values calculated for a combination of

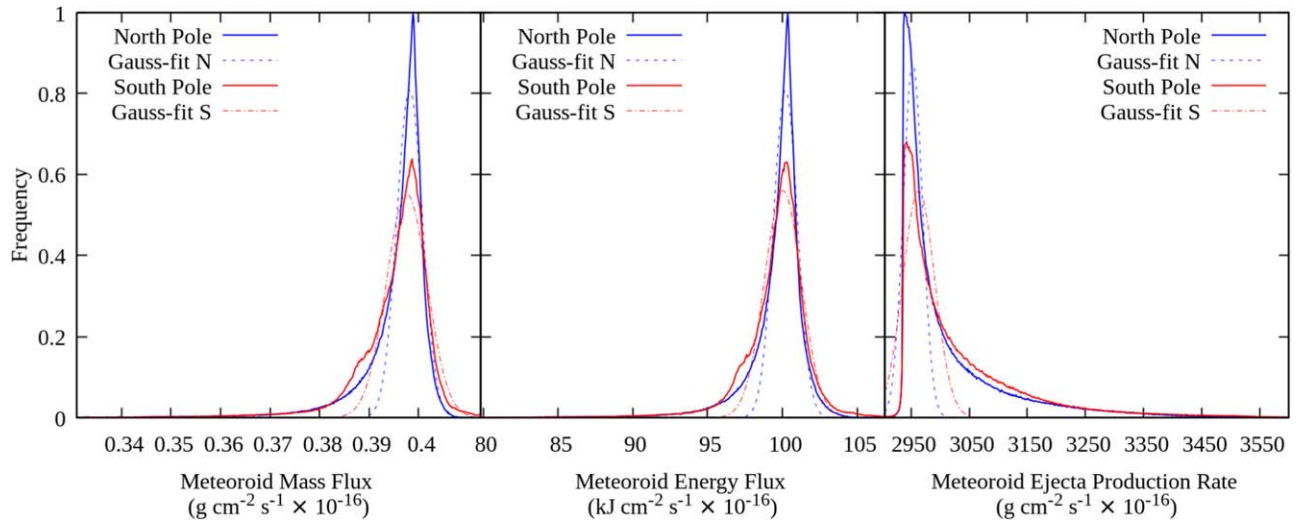


Figure 3. Frequencies of occurrences for \mathcal{M} (left panel), \mathcal{E} (middle panel) and \mathcal{P}^+ (right panel) normalized to the maximum frequency on either poles. Blue solid lines indicate values for the north pole, whereas blue dashed lines are Gaussian fits to their respective quantities. Red lines show their south pole equivalents.

Table 2

Coefficients for Quadratic Function Fits ($f(x) = ax^2 + bx + c$) of the Meteoroid Ejecta Production Rate vs. Slope Dependency for Both the North and South Lunar Poles

	South			North		
	a	b	c	a	b	c
5% percentile	0.5078	-3.4082	2941.2	0.5350	-3.8322	2941.7
50% percentile	0.4978	2.7356	2942.7	0.6682	0.0638	2946.4
95% percentile	0.6443	7.4543	2956.2	0.6147	7.4240	2956.5

Table 3

Median Values for \mathcal{M} ($\text{g cm}^{-2} \text{s}^{-1} \times 10^{-16}$), \mathcal{E} ($\text{kJ cm}^{-2} \text{s}^{-1} \times 10^{-16}$), and \mathcal{P}^+ ($\text{g cm}^{-2} \text{s}^{-1} \times 10^{-16}$) for Both Lunar Poles Differentiated by Four Meteoroid Source Populations

	MBA	JFC	HTC	OCC
Median Value				
\mathcal{M}	0.0264	0.2595	0.0682	0.0431
\mathcal{E}	1.1618	30.724	35.325	32.700
\mathcal{P}^+	33.476	737.88	1334.6	891.94
Percentage (%)				
\mathcal{M}	6.6465	65.332	17.170	10.851
\mathcal{E}	1.1628	30.751	35.357	32.729
\mathcal{P}^+	1.1166	24.614	44.517	29.753
Normalized to 1000 kg per day at Earth (%)				
\mathcal{M}	12.178	12.801	41.277	33.744
\mathcal{E}	1.0932	3.0909	43.603	52.213
\mathcal{P}^+	0.9912	2.3364	51.847	44.825

Note. The middle rows show percentages for each population. The bottom rows show percentages for each population normalized to 1000 kg per day for each source population. The calibrated mass flux at Earth used here is adopted from MBA = 3700, JFC = 34,600, HTC = 2820, and OCC = 2180 kg per day.

both poles show that JFC meteoroids dominate the meteoroid mass flux \mathcal{M} by providing 65% of the total sum. However, this percentage changes for both the meteoroid energy flux \mathcal{E} where HTC meteoroids lead with 35%, followed by OCC meteoroids with 33% and JFC meteoroids with 31%. This change is due to

the higher impact velocities of HTC and OCC meteoroids. \mathcal{P}^+ follows a similar trend with HTC meteoroids acquiring almost 45% of the total sum due to their larger spread in ecliptic latitudes and thus easier access of both lunar poles. With the exception of the meteoroid mass flux where MBA meteoroids represent 7% of the total mass flux, the energy flux and ejecta production rates are close to 1% and thus the MBA contribution can be neglected.

The meteoroid environment bombarding the moon is calibrated using the terrestrial mass flux with the following values: MBA = 3700, JFC = 34,600, HTC = 2820, and OCC = 2180 kg per day (Carrillo-Sánchez et al. 2016; Pokorný et al. 2019). In order to better quantify the effects of the meteoroid impact geometry and lunar topography, we normalized the terrestrial mass flux for each meteoroid source to 1000 kg per day (bottom part of Table 3). The normalized mass flux is very similar for MBA and JFC meteoroids (12%–13%) but the long-period comet sources are much more efficient in delivering mass to the lunar poles since their ecliptic latitudes spread further from the ecliptic. Furthermore, due to their higher impact velocities, the long-period sources dominate both \mathcal{E} and \mathcal{P}^+ with >95% of the total from all sources. Only due to their abundance in the inner solar system, JFC meteoroids are a significant contributor to the space weathering processes on lunar poles.

How is it possible to achieve such uniform distributions of the mass flux, energy flux, or ejecta production rate over such a variable topography? Pokorný et al. (2019) showed that the meteoroids impacting the Moon have a very broad distribution of the ecliptic latitude (i.e., the angular distance measured from

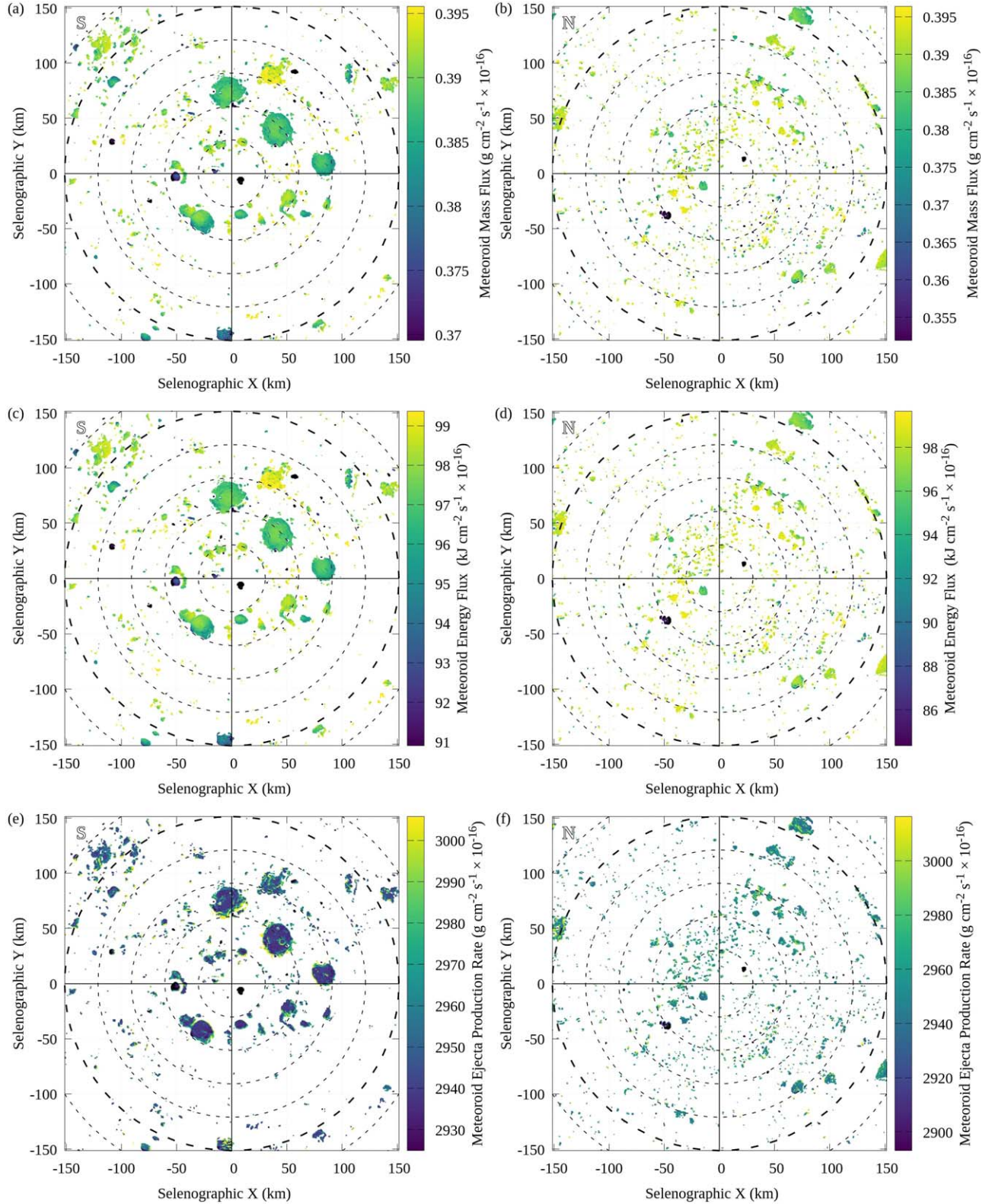


Figure 4. The same as Figure 1 but now only for low slope ($<10^\circ$) water-ice stable ($T_{\text{max}} < 110$ K) regions.

the ecliptic in the z -direction), thus even deep polar craters are exposed to a considerable meteoroid flux, especially the north/south toroidal source observed at Earth (Campbell-Brown 2008; Janches et al. 2015) originating from long-period comets (Nesvorný et al. 2011; Pokorný et al. 2014). Moreover, the

abundant and high-energy meteoroid sources close to the ecliptic impact the lunar poles at very shallow angles, and due to the cosine dependence, their contribution will be considerably diminished. This effect is even more accentuated for the ejecta mass production rates \mathcal{P}^+ due to the steeper dependency

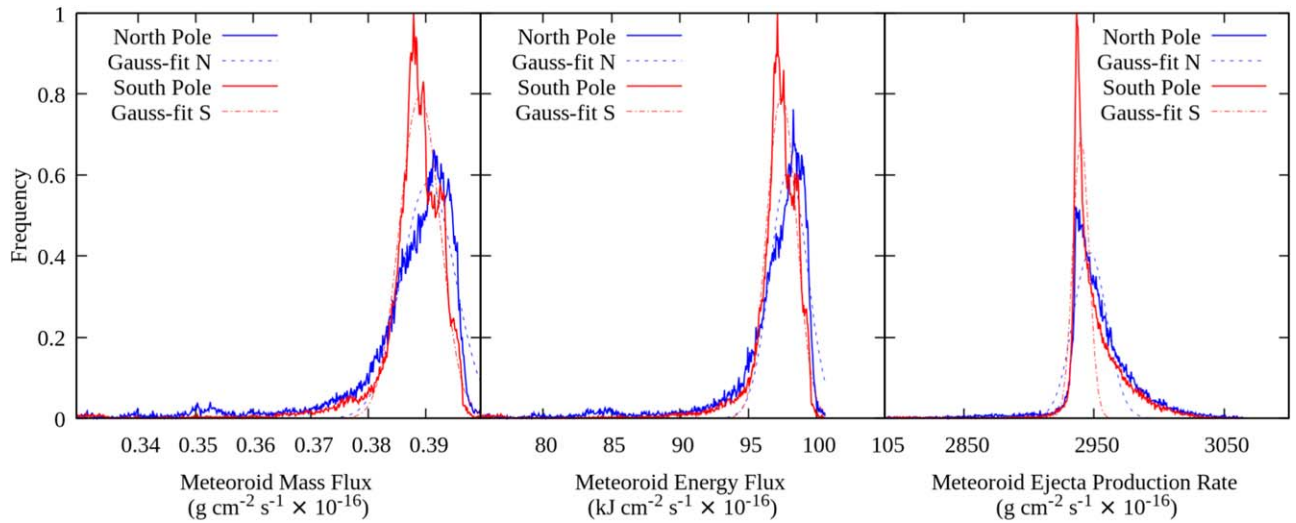


Figure 5. The same as Figure 3 but now only for low slope ($<10^\circ$) water-ice stable ($T_{\max} < 110$ K) regions.

on the incidence angle (see, e.g., Gault 1973) and thus the locations with small slopes experience negligible contributions from low-inclination meteoroids.

5. Permanently Shadowed Regions with Low Slopes—Regions Without Mass Wasting

In this section we focus on regions that should be unaffected by mass wasting and should be able to sustain water-ice deposits for geological timescales. For such regions we choose the surface slope $\alpha < 10^\circ$ based on work of Lucey et al. (2014), who concluded that $\alpha < 10^\circ$ is safe from mass wasting. Furthermore we analyze only regions where the maximum surface temperature $T_{\max} < 110$ K, i.e., regions that should be able to sustain ice deposits for geological timescales. Independent remote spacecraft sensing data from the Moon Mineralogy Mapper (Li et al. 2018) and LRO (Fisher et al. 2017) show that many of these regions should indeed harbor deposits of water-ice.

The motivation for a more detailed analysis of such regions stems from the recent works regarding space weathering and surface regolith alteration in and around south pole craters that are partially shadowed and partially exposed to solar irradiation and solar wind (Byron et al. 2019). Such places, that are unique only to polar regions, are fortuitous laboratories allowing us to study different processes of lunar soil alteration separately. Mass wasting on more inclined slopes exposes the fresh, unweathered material (e.g., Zuber et al. 2012), which effectively restarts the space weathering process and adds complexity into the soil alteration analysis.

Figure 4 shows the variations of \mathcal{M} , \mathcal{E} , and \mathcal{P}^+ for all regions that satisfy our conditions. We see that the topography of the north and south poles is very different, where in the south the flat, cold, and stable areas (CSAs) are mostly concentrated in several craters, while at the north pole CSAs are more scattered and also less abundant (approximately 4500 km^2 versus 2130 km^2 for south and north respectively). Despite significant differences in the CSA distribution at both locations, the mass flux distribution is very similar for both lunar poles, which is more clearly shown in the frequency histograms (Figure 5). When compared to Figure 3, the distributions are shifted toward the lower values due to being shadowed from the low-inclination meteoroid impacts,

however the median values are only 2% smaller than the median values calculated for the entire map. Only craters with high slope angles $\sim 30^\circ$, like Shackleton, are shielded more efficiently, however neither the mass flux nor the energy flux decrease by more than 20% below the median values.

The meteoroid ejecta production rate exhibits somewhat more variation, but within different craters it does not reach more than a few percent. We conclude that the ice deposits should not exhibit significantly different aging signatures due to the meteoroid impacts. Perhaps the more important effect is the meteoroid-induced mass wasting from the crater sides with higher slopes. In these places the rims are being excavated significantly more efficiently than the floor, and the material excavated from the crater sides may be flowing into the crater and burying the top layers of its floor. Ejecta trajectories and model mass wasting caused by meteoroids might be investigated in future work.

6. Discussion

The meteoroid dynamical model used here (Pokorný et al. 2019) is a product of several years of work that combines the dynamical evolution of meteoroid-generating populations in the solar system (main-belt asteroids, short-/long-period comets) and various observed constraints. The meteoroid model has inherent uncertainties due to the complex nature of both the dynamical modeling and its intrinsic free parameters, as well as the uniqueness of each constraint (meteor orbital distribution at Earth, shape of the Zodiacal cloud, spacecraft measured particle flux). Pokorný et al. (2019) quantified the effect of several free parameters in their model, showing it to be quite robust to such uncertainty. The three most influential free parameters in their models were found to be: (a) the collisional lifetime multiplier, F_{coll} , that effectively scales the flux of meteoroids with diameters $D > 200 \mu\text{m}$ (see Figure 6 in Pokorný et al. 2019); (b) the differential size–frequency index α that scales the relative abundance of meteoroids ejected from their sources; and (c) the mixing of meteoroid populations at Earth. The effects of different combinations of (a) $F_{\text{coll}} \in [10, 50]$ and (b) $\alpha \in [3.4, 4.6]$ was $\pm 10\%$ with respect to the overall mass flux on the Moon, and about $\pm 17\%$ in terms of the energy flux. These variations were with respect to the entire surface of the Moon. When only

the polar regions are taken into account, the maximum divergence from the model solution used in this study is $<10\%$ for all three main quantities considered here: \mathcal{M} , \mathcal{E} , and \mathcal{P}^+ .

The population mixing (i.e., the ratio between asteroidal and cometary sources) adopted here relies strongly on the work reported by Carrillo-Sánchez et al. (2016) and LDEX measurements that Pokorný et al. (2019) used to constrain the ratio of HTC and OCC. Here, we present the results as the currently best dynamical model we can provide. Should a new set of constraints emerge that would significantly change the quantities investigated here, the model could be updated in the future.

Even though meteoroid gardening might be the dominant source of surface water-ice removal on lunar poles (Hayne et al. 2015), there is no significant difference in the distribution of the meteoroid flux or meteoroid ejecta production rate between the two lunar poles based on our calculations. One factor that might change the absolute values of meteoroid ejecta production rates presented here by orders of magnitude are the assumed ejecta yields. Due to the lack of experiments at speeds $V_{\text{imp}} \gtrsim 10 \text{ km s}^{-1}$, we can only speculate on the effects of higher impact velocities to the ejecta rate from different surface materials. However, the comparison of the meteoroid impact generated ejecta to the lunar dust cloud density in Pokorný et al. (2019) suggests that the regolith ejecta yield might be orders of magnitude smaller than that of ice–silicate surfaces used in Koschny & Grün (2001). This effect could potentially have major consequences on the excavation of pure ice deposits in PSRs, because pure ice or surface-exposed ice would be excavated on shorter timescales than ice–regolith mixtures or pure regolith layers. Thus the differences in ejecta yields between different materials might be more important than differences in meteoroid access to these regions. Although beyond the scope of this article, it should be possible to quantify the erosion of different regions showing water-ice signatures using the calculations presented here.

Haruyama et al. (2013) tackled the problem of the water-ice presence inside the Shackleton crater by analyzing the Selenological Engineering Explorer mission observations and concluded that the high reflectance regions inside the crater are due to the presence of pure anorthosite. Zuber et al. (2012) provided an alternative explanation that the LRO LOLA reflectance could be explained by 20% water-ice content. In Figure 1 we showed that the internal part of the Shackleton crater is subject to higher meteoroid ejecta production rates because high slopes are more susceptible to high-energy impacts, which suggests increased mass wasting on Shackleton’s inner walls. Such impacts should excavate fresh material that might be transported deeper into the crater. This idea is also supported by the depletion in craters on both Shackleton’s rim and floor (Tye et al. 2015), which is most likely caused by extensive mass wasting induced by meteoroid impacts.

Even though the impact driven excavation of water-ice is a complex mechanism and its modeling is beyond the scope of this article, initial estimates can be made from the quantities presented in Figure 1. The meteoroid energy flux $\mathcal{E} = 100 \times 10^{-16} \text{ kJ cm}^{-2} \text{ s}^{-1}$ can be converted to the impact vaporization rate, $\mathcal{V} = 6 \times 10^{-16} \text{ g cm}^{-2} \text{ s}^{-1}$, using iron projectiles, a temperature of 400 K, and the quadratic term from Equation 10 in Cintala (1992). Assuming the regolith bulk density $\rho = 1.5 \text{ g cm}^{-3}$, the impacts vaporize $4.5 \times 10^{-16} \text{ mm s}^{-1}$, which

translates to $1.3 \times 10^{-7} \text{ mm yr}^{-1}$. Morgan & Shemansky (1991) state that the local interstellar medium H Ly α radiation is the most efficient destruction process of water-ice which amounts to $7 \times 10^{-8} \text{ mm per year}$, i.e. an effect comparable in magnitude to meteoroid bombardment. Both effects are not significantly affected by the polar topography, thus a proper modeling of impact gardening is needed to fully cover all subtle effects that regulate the water-ice stability on lunar poles.

7. Conclusions

We present the first quantification of the meteoroid mass flux, meteoroid energy flux, and meteoroid ejecta production rate based on dynamical models and reflecting the topography of both lunar poles. The main conclusions can be summarized as follows.

1. Despite the complex topography of lunar poles and the presence of many permanently shadowed regions, the meteoroid-induced processes are rather uniform, with maximum deviations of 30% from the median values of these quantities.
2. Unlike the solar wind, meteoroid impacts can provide the energy needed for surface weathering (e.g., formation of nanophase iron, band-depth reduction) even at the deepest polar craters.
3. The local meteoroid ejecta production rate can be expressed as a second-degree polynomial function of the surface slope, where the higher surface slopes are subject to higher excavation rates by meteoroids from long-period comets. This result promotes substantial mass wasting.
4. Crater walls with high slopes such as Shackleton are being constantly reprocessed by the meteoroid bombardment, which exposes fresher material. Additionally, as a result of the efficient mass wasting, the material on the floor of such craters will be buried by both the constant meteoroid mass flux and the material sliding from the crater walls.
5. Due to small variations of meteoroid bombardment effects, we suggest that different excavation rates of ice deposits are due to different ejecta yields of various mixtures of ice–regolith surface layers.

The relative uniformity of meteoroid-induced processes from crater to crater results from the finding that the meteoroid environment of the Moon is composed of meteoroids with a broad range of inclinations which reduces the shadowing effects. If more pronounced differences across craters are attributable to meteoroid impacts than shown here, such a finding could imply higher relative importance of long-period comets presently or in the past. Such differences might also arise from significant differences in ejecta yields for different materials (e.g., ice-free soils versus ice).

All quantities calculated in this work for both lunar poles are available at https://github.com/McFly007/AstroWorks/tree/master/Pokorny_et_al_2019_ApJ and cover a $300 \text{ km} \times 300 \text{ km}$ area centered at both poles, i.e., approximately 5° away from the pole. We combined our data set with the Diviner output for convenience, so the values of the maximum temperature, average temperature, albedo, and depth of ice are readily available. The complete description of the data products can be found in the project directory together with future updates.

P.P.’s, D.J.’s and M.S.’s work was supported with NASA’s SSO, LDAP, and ISFM awards. The data products, codes and data

used to generate plots in this manuscript can be found at https://github.com/McFly007/AstroWorks/tree/master/Pokorny_et_al_2019_ApJ.

Appendix A Data Set Overview

Topography

The reference for these data sets is Smith et al. (2017). LRO LOLA GDR in polar stereographic projection for the south lunar pole (240 m^{-1}) resolution: http://imbrium.mit.edu/DATA/LOLA_GDR/POLAR/FLOAT_IMG/LDEM_75S_240M_FLOAT.IMG.

LRO LOLA GDR in polar stereographic projection for the north lunar pole (240 m^{-1}) resolution: http://imbrium.mit.edu/DATA/LOLA_GDR/POLAR/FLOAT_IMG/LDEM_75N_240M_FLOAT.IMG.

Average Temperatures, Maximum Temperatures, Depth to Water-ice Permafrost

The reference for these data sets is Paige et al. (2010). LRO Diviner Lunar Radiometer Polar Resource Products—south lunar pole: http://pds-geosciences.wustl.edu/lro/lro-l-dlre-4-rdr-v1/lrodlr_1001/data/prp/dlre_prp_south.tab.




LRO Diviner Lunar Radiometer Polar Resource Products—north lunar pole: http://pds-geosciences.wustl.edu/lro/lro-l-dlre-4-rdr-v1/lrodlr_1001/data/prp/dlre_prp_north.tab.

Albedo

The reference for these data sets is Lemelin et al. (2016). LRO LOLA surface albedo maps in polar stereographic projection for the south lunar pole (1000 m pixel^{-1}) resolution: http://imbrium.mit.edu/DATA/LOLA_GDR/POLAR/FLOAT_IMG/LDAM_50S_1000M_FLOAT.IMG.

LRO LOLA surface albedo maps in polar stereographic projection for the north lunar pole (1000 m^{-1}) resolution: http://imbrium.mit.edu/DATA/LOLA_GDR/POLAR/FLOAT_IMG/LDAM_50N_1000M_FLOAT.IMG.

ORCID iDs

Petr Pokorný  <https://orcid.org/0000-0002-5667-9337>
Menelaos Sarantos  <https://orcid.org/0000-0003-0728-2971>
Diego Janches  <https://orcid.org/0000-0001-8615-5166>
Erwan Mazarico  <https://orcid.org/0000-0003-3456-427X>

References

- Arnold, J. R. 1975, *LPSC*, **2**, 2375
Byron, B. D., Retherford, K. D., Greathouse, T. K., et al. 2019, *JGRE*, **124**, 823
Campbell-Brown, M. D. 2008, *Icar*, **196**, 144
Carrillo-Sánchez, J. D., Nesvorný, D., Pokorný, P., Janches, D., & Plane, J. M. C. 2016, *GeoRL*, **43**, 11
Cintala, M. J. 1992, *JGR*, **97**, 947
Colaprete, A., Schultz, P., Heldmann, J., et al. 2010, *Sci*, **330**, 463
Deutsch, A. N., Head, J. W., & Neumann, G. A. 2020, *Icar*, **336**, 113455
Fisher, E. A., Lucey, P. G., Lemelin, M., et al. 2017, *Icar*, **292**, 74
Gault, D. E. 1973, *Moon*, **6**, 32
Haruyama, J., Yamamoto, S., Yokota, Y., Ohtake, M., & Matsunaga, T. 2013, *GeoRL*, **40**, 3814
Hayne, P. O., Hendrix, A., Sefton-Nash, E., et al. 2015, *Icar*, **255**, 58
Horányi, M., Szalay, J. R., Kempf, S., et al. 2015, *Natur*, **522**, 324
Hurley, D. M., Lawrence, D. J., Bussey, D. B. J., et al. 2012, *GeoRL*, **39**, L09203
Janches, D., Close, S., Hormaechea, J. L., et al. 2015, *ApJ*, **809**, 36
Koschny, D., & Grün, E. 2001, *Icar*, **154**, 402
Lemelin, M., Lucey, P. G., Neumann, G. A., et al. 2016, *Icar*, **273**, 315
Li, S., Lucey, P. G., Milliken, R. E., et al. 2018, *PNAS*, **115**, 8907
Li, S., & Milliken, R. E. 2017, *SciA*, **3**, e1701471
Lucey, P. G., Neumann, G. A., Riner, M. A., et al. 2014, *JGRE*, **119**, 1665
Mazarico, E., Barker, M. K., & Nicholas, J. B. 2018, *AdSpR*, **62**, 3214
Morgan, T. H., & Shemansky, D. E. 1991, *JGR*, **96**, 1351
Nesvorný, D., Vokrouhlický, D., Pokorný, P., & Janches, D. 2011, *ApJ*, **743**, 37
Paige, D. A., Foote, M. C., Greenhagen, B. T., et al. 2010, *SSRv*, **150**, 125
Pokorný, P., Janches, D., Sarantos, M., et al. 2019, *JGRE*, **124**, 752
Pokorný, P., Vokrouhlický, D., Nesvorný, D., Campbell-Brown, M., & Brown, P. 2014, *ApJ*, **789**, 25
Rubanenko, L., Venkatraman, J., & Paige, D. A. 2019, *NatGe*, **12**, 597
Smith, D. E., Zuber, M. T., Neumann, G. A., et al. 2010, *GeoRL*, **37**, L18204
Smith, D. E., Zuber, M. T., Neumann, G. A., et al. 2017, *Icar*, **283**, 70
Suggs, R. M., Moser, D. E., Cooke, W. J., & Suggs, R. J. 2014, *Icar*, **238**, 23
Tye, A. R., Fassett, C. I., Head, J. W., et al. 2015, *Icar*, **255**, 70
Zuber, M. T., Head, J. W., Smith, D. E., et al. 2012, *Natur*, **486**, 378